Chemical Science

EDGE ARTICLE

View Article Online
View Journal

Check for updates

Cite this: DOI: 10.1039/d6sc01645f

All publication charges for this article have been paid for by the Royal Society of Chemistry

Received 26th February 2026
Accepted 28th April 2026

DOI: 10.1039/d6sc01645f

rsc.li/chemical-science

Engineering hydrophobic covalent organic frameworks for electroreduction of nitrate to ammonia

Fuzhen Li,[a] Huan Lin,[c] Chunying Chen,[c] Li-Lin Tan,[b] Dawei Wang,[c] Cunyuan Zhao,[c] Li Zhang *[c] and Cheng-Yong Su[c]

The development of efficient electrocatalysts for the nitrate reduction reaction (NO_3RR) to ammonia is crucial for sustainable nitrogen management, but remains challenging due to its intricate multi-step mechanism and competing side reactions. A key bottleneck is the severe imbalance between the generation and consumption of H*, which critically constrains ammonia selectivity and yield. Herein, a molecular engineering strategy was developed through the incorporation of Pd-porphyrin to promote the generation of H*, while grafting ethoxyphenyl groups to create a hydrophobic microenvironment and inhibit the hydrogen evolution reaction. The covalent organic framework of Pd-PCOF-2(Cu_3), which was prepared from the reaction of Pd(II) diaminoporphyrin and trinuclear copper cluster aldehyde, achieved a high NH_3 faradaic efficiency of 94.7% and a production rate of 15.09 mg h^{-1} cm^{-2}. A rechargeable Zn–NO_3^- battery with Pd-PCOF-2(Cu_3) as the cathode was further constructed, which served as a dual-function system for both power output and ammonia production.

Introduction

Ammonia (NH_3) is a pivotal chemical commodity in modern society, which serves not only as the fundamental feedstock for the fertilizer industry but is also regarded as a promising future energy carrier due to its high energy density and carbon-free nature.[1,2] Currently, industrial ammonia synthesis still predominantly relies on the conventional Haber–Bosch process with harsh conditions of high temperature (350–550 °C) and high pressure (15–25 MPa), which is associated with substantial energy consumption, significant carbon emissions and a deep reliance on fossil fuels, starkly contradicting the global "carbon neutrality" goal.[3] In this context, the direct electrochemical reduction of atmospheric nitrogen (NRR) to ammonia, utilizing renewable electricity and water as the proton source, has garnered significant research interest due to its mild operating conditions and environmentally friendly characteristics. However, its practical application is severely limited by the extremely high dissociation energy of the N≡N triple bond (941 kJ mol^{-1}) and the low solubility of N_2 in aqueous solutions (~0.6 mM), resulting in poor reaction kinetics and negligible yield.[4,5]

Inspired by the comparatively lower dissociation energy of NO_3^- (204 kJ mol^{-1}) and its high solubility, the formation of NH_3 from the electrocatalytic nitrate reduction reaction (NO_3RR) has emerged as a compelling alternative strategy.[6–8] Nevertheless, the NO_3RR process involves a complex multi-step mechanism encompassing an eight-electron, nine-proton transfer pathway ($NO_3^- + 9H^+ + 8e^- \rightarrow NH_3 + 3H_2O$), with the sequential hydrogenation/deoxygenation step of NO_3^- and critical intermediates such as nitrite (NO_2^-) driven by active hydrogen (H*) from H_2O decomposition/reduction.[9,10] Hence, the supply and utilization of H* play a pivotal role.[11,12] An inadequate supply of H* can kinetically limit the hydrogenation steps, leading to the accumulation of reaction intermediates and reduced efficiency. Conversely, an over-abundance of H* readily promotes H–H coupling, triggers the competing hydrogen evolution reaction (HER) and lowers the faradaic efficiency for NH_3. Therefore, the precise regulation of the H* supply to couple with the specific hydrogenation steps of the nitrate reduction pathway is crucial for achieving optimal performance.[13,14] Some strategies to address this issue have been reported, including single-atom alloys, dual-atom catalysts and heterojunction engineering.[15–20] Given that hydrophobicity can limit the accumulation of water molecules at the catalyst surface and thus suppress the HER, the rational construction of a hydrophobic microenvironment to precisely regulate the supply of H* represents a feasible strategy.[21] So far, its application in the field of electrocatalytic NO_3RR has been underdeveloped.

Owing to the precise structural tunability and robust covalent architectures, covalent organic frameworks (COFs) display

---

[a] *School of Chemical Engineering and Technology, Sun Yat-sen University, Zhuhai 519082, China*

[b] *Shantou Engineering Technology Research Center for Green and Precise Manufacturing of High-value Chemicals, Chemistry and Chemical Engineering Guangdong Laboratory, Shantou 515031, China*

[c] *Lehn Institute of Functional Materials, School of Chemistry, Sun Yat-Sen University, Guangzhou 510006, China. E-mail: zhli99@mail.sysu.edu.cn*

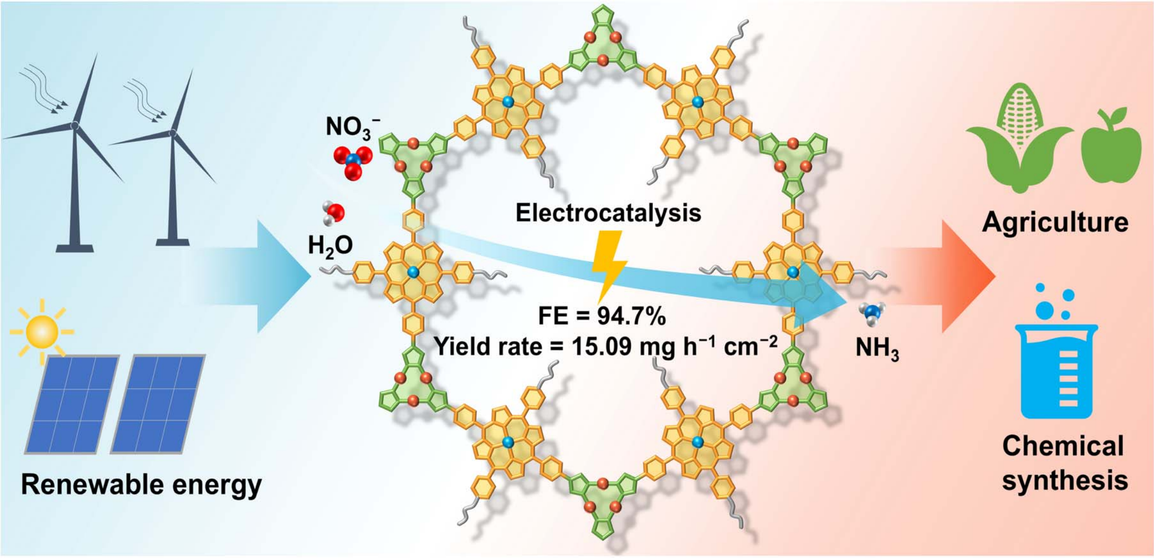

Fig. 1 Schematic illustration of electrocatalytic NO_3RR by Pd-PCOF-2(Cu_3).

advantages in electrocatalytic reactions, especially under alkaline conditions.[22–28] Porphyrins possess conjugated structures and excellent electrical properties, and are thus employed as pivotal building blocks and active sites in the construction of porphyrin-based COFs (PCOFs) for electrocatalytic applications.[29–35] Furthermore, the single-metal site within the metalloporphyrin is pivotal for the formation of M–H (metal–hydride) active species, which could assist in the electrocatalytic reduction of NO_3^- to NH_3.[36,37] Nevertheless, the vast majority of reported PCOFs are structurally limited to *sql* topology derived from C_4-symmetric tetraphenylporphyrin building blocks. Consequently, not only the promising strategy of porphyrin side-chain engineering for PCOFs remains largely unexplored, but also the design and construction of new PCOF topologies merit further investigation.

Herein, three new A_2B_2-type diaminoporphyrin monomers were designed and synthesized, which subsequently reacted with a trinuclear copper cluster (Cu_3) aldehyde ligand *via* Schiff-base condensation, giving rise to three two-dimensional imine-linked PCOFs with ABC stacking and a hcb topology, denoted as Pd-PCOF-1(Cu_3), Pd-PCOF-2(Cu_3), and PCOF-2(Cu_3), respectively. On one hand, the precise integration of hydrophobic phenyl or ethoxyphenyl side groups of porphyrins engineered a pore-confined hydrophobic microenvironment. On the other hand, the introduction of Pd centers within the porphyrin macrocycles, alongside the Cu_3, established well-defined bimetallic active sites. This deliberate architectural design facilitated exceptional electrocatalytic performance for the NO_3RR under alkaline conditions. Catalytic results showed that Pd-PCOF-2(Cu_3) achieved a remarkable faradaic efficiency up to 94.7% and a high NH_3 generation rate of 15.09 mg h^{-1} cm^{-2} at applied potentials of −1.0 V and −1.1 V *vs.* RHE, respectively. It also maintained stable performances over 10 consecutive catalytic cycles, ranking among the top reported COF/MOF-based electrocatalysts (Table S1). Mechanistic investigations revealed that the hydrophobic microenvironment played a critical role in precisely regulating the supply of H*, which could effectively suppress the competing HER. Concurrently, the Cu_3 and Pd centers served as the catalytic sites for the adsorption/activation of NO_3^- and the hydrogenation of the NO_2^- intermediate, respectively, forming an efficient bimetallic synergistic catalytic mechanism, which minimized the accumulation of NO_2^-, enhanced the overall reaction rate, and optimized NO_3^- to NH_3 conversion (Fig. 1).

Experimental

Synthesis of 5,15-diphenyl-10,20-bis(4-nitrophenyl) porphyrin (DNPP)

Prior to the synthesis of DNPP, 2,2′-((4-nitrophenyl)methylene) bis(1H-pyrrole) (NPBPR) was prepared (Fig. S1 and S2). And then, NPBPR (5.34 g, 0.02 mol), benzaldehyde (2.12 g, 0.02 mol) and propionic acid (300 mL) were mixed in a 500 mL round-bottom flask. The mixture was stirred at 140 °C for 2 h and then cooled down to room temperature. After propionic acid was removed under reduced pressure, the crude product was purified by column chromatography (silica, CH_2Cl_2/MeOH 49 : 1) to afford DNPP as a purple solid (0.78 g, 11% yield).

Synthesis of 5,15-bis(4-ethoxyphenyl)-10,20-bis(4-nitrophenyl) porphyrin (EDNPP)

EDNPP was synthesized using a procedure similar to that of DNPP, except that benzaldehyde was replaced by 4-ethoxybenzaldehyde (3.0 g, 0.02 mol). EDNPP was obtained as a purple solid (0.95 g, 12% yield).

Synthesis of 5,15-bis(4-ethoxyphenyl)-10,20-bis(4-aminophenyl)porphyrin (EDAPP)

EDNPP (0.317 g, 0.4 mmol), stannous chloride dihydrate ($SnCl_2 \cdot 2H_2O$, 0.36 g, 1.6 mmol), tetrahydrofuran (THF, 70 mL) and concentrated hydrochloric acid (HCl, 10 mL) were mixed in a 250 mL round-bottom flask. The mixture was stirred at 70 °C for 2 h and then cooled down to room temperature. After the excess HCl was neutralized with ammonia water, the mixture was extracted with CH_2Cl_2. The organic layer was collected, dried over Na_2SO_4 and concentrated under reduced pressure. Subsequently, the crude product was purified by column chromatography (silica, CH_2Cl_2/MeOH 49 : 1) to afford EDAPP as a purple solid (0.264 g, 90% yield). ^1H NMR (400 MHz, DMSO-d_6, Fig. S3) δ 8.92 (d, $J = 4.8$ Hz, 4H), 8.82 (d, $J = 4.8$ Hz, 4H), 8.11 (d, $J = 8.4$ Hz, 4H), 7.85 (d, $J = 8.1$ Hz, 4H), 7.37 (d, $J = 8.5$ Hz, 4H), 7.01 (d, $J = 8.3$ Hz, 4H), 5.57 (s, 4H), 4.35 (q, $J = 6.9$ Hz, 4H), 1.54 (t, $J = 6.9$ Hz, 6H), −2.79 (s, 2H).

Synthesis of Pd(II)-5,15-diphenyl-10,20-bis(4-nitrophenyl) porphyrin (Pd-DNPP)

DNPP (0.35 g, 0.5 mmol), palladium chloride ($PdCl_2$, 0.35 g, 2 mmol) and DMF (200 mL) were mixed in a 500 mL round-bottom flask. The mixture was stirred at 160 °C for 12 h and then cooled down to room temperature. After DMF was removed under reduced pressure, the crude product was purified by column chromatography (silica, CH_2Cl_2/MeOH 49 : 1) to afford Pd-DNPP as a reddish purple solid (0.364 g, 90% yield).

Synthesis of Pd(II)-5,15-bis(4-ethoxyphenyl)-10,20-bis (4-nitrophenyl)porphyrin (Pd-EDNPP)

Pd-EDNPP was synthesized using a procedure similar to that of Pd-DNPP, except that DNPP was replaced by EDNPP (0.396 g, 0.5 mmol). Pd-EDNPP was obtained as a reddish purple solid (0.412 g, 92% yield).

Synthesis of Pd(II)-5,15-diphenyl-10,20-bis(4-aminophenyl) porphyrin (Pd-DAPP)

Pd-DAPP was synthesized using a procedure similar to that of EDAPP, except that EDNPP was replaced by Pd-DNPP (0.32 g, 0.4 mmol). Pd-DAPP was obtained as a reddish purple solid (0.282 g, 94% yield). ^1H NMR (400 MHz, DMSO-d_6, Fig. S4) δ 8.93 (d, $J = 5.0$ Hz, 4H), 8.75 (d, $J = 4.9$ Hz, 4H), 8.18 (d, $J = 5.2$ Hz, 4H), 7.92–7.73 (m, 10H), 6.99 (d, $J = 8.0$ Hz, 4H), 5.56 (s, 4H).

Synthesis of Pd(II)-5,15-bis(4-ethoxyphenyl)-10,20-bis (4-aminophenyl)porphyrin (Pd-EDAPP)

Pd-EDAPP was synthesized using a procedure similar to that of Pd-DAPP, except that Pd-DNPP was replaced by Pd-EDNPP (0.358 g, 0.4 mmol). Pd-EDAPP was obtained as a reddish purple solid (0.295 g, 88% yield). ^1H NMR (400 MHz, DMSO-d_6, Fig. S5) δ 8.92 (d, $J = 4.9$ Hz, 4H), 8.81 (d, $J = 5.0$ Hz, 4H), 8.08 (d, $J = 8.4$ Hz, 4H), 7.81 (d, $J = 8.1$ Hz, 4H), 7.36 (d, $J = 8.3$ Hz, 4H), 7.00 (d, $J = 8.2$ Hz, 4H), 5.58 (s, 4H), 4.35 (q, $J = 7.1$ Hz, 4H), 1.55 (t, $J = 6.9$ Hz, 6H).

Synthesis of Pd-PCOF-1(Cu_3)

Pd-DAPP (22.47 mg, 0.03 mmol), $Cu_3(PyCA)_3$ (9.52 mg, 0.02 mmol), *n*-butanol (*n*-BuOH, 0.5 mL) and *o*-dichlorobenzene (*o*-DCB, 0.5 mL) were sequentially added to a 10 mL Schlenk tube and sonicated for 5 min. Subsequently, TFA (6 M, 0.1 mL) was added to the tube and sonicated for 5 min, and then the tube was degassed and heated at 120 °C for 3 days. The precipitated solid was collected by centrifugation and washed sequentially with THF, DMF and acetone several times. The solids were dried at 100 °C for 12 h to afford Pd-PCOF-1(Cu_3) (27 mg, 85% yield) as red powders.

Synthesis of Pd-PCOF-2(Cu_3) and PCOF-2(Cu_3)

The synthesis procedure for Pd-PCOF-2(Cu_3) and PCOF-2(Cu_3) was similar to that of Pd-PCOF-1(Cu_3), except that Pd-EDAPP and EDAPP were used instead of Pd-DAPP. Pd-PCOF-2(Cu_3) (30 mg, 86% yield) and PCOF-2(Cu_3) (22.3 mg, 71% yield) were obtained as red and brown powders, respectively.

Electrochemical measurements

To prepare the working electrodes, 10 mg of the as-prepared catalyst, 5 mg of acetylene black, and 50 μL of Nafion solution (5 wt%) were dispersed in 450 μL of isopropanol (IPA) and sonicated for 30 min to give a homogeneous catalyst ink. Subsequently, 50 μL of the catalyst ink was dropped on a hydrophobic carbon cloth with an area of 1 cm^2 (the area of carbon cloth was 1×2 cm^2) and dried at 80 °C for 1 h to achieve a catalyst areal loading of 1 mg cm^{-2}. Electrochemical NO_3RR measurements were carried out with a standard three-electrode system using a typical H-type electrolytic cell separated by a Nafion 117 membrane at room temperature and atmospheric pressure. The H-cell experiment was conducted on a CHI 660E workstation (Shanghai Chenhua), equipped with a platinum plate counter electrode and an Hg/HgO (with 1 M KOH solution) reference electrode. All the potentials in the measurements were converted to the reversible hydrogen electrode (RHE) scale according to the equation: Potential $= E_{Hg/HgO} + 0.0592$ pH + 0.098 V (pH = 14 for 1 M KOH). The electrolyte (60 mL 1 M KOH) was evenly distributed between the cathode and anode compartments, and 0.1 M KNO_3 was added only to the cathode compartment. Before the electrochemical measurement, the electrolyte of the cathode compartment was purged with 20 sccm of high-purity Ar (99.999%) for 10 min to remove dissolved O_2, and the flow rate of Ar was adjusted to 10 sccm during the measurement. Linear sweep voltammetry (LSV) was performed at a scan rate of 10 mV s^{-1}. The chronoamperometry test was performed at 0.1 V intervals from −0.6 V to −1.1 V *vs.* RHE for 1000 s under a constant stirring rate of 800 rpm, and the products (NH_3, NO_2^- and H_2) were determined quantitatively separately. For the cycle stability test, the chronoamperometry test was performed at −0.9 V *vs.* RHE for 1000 s and using the fresh electrolyte for every cycle. Electrochemical impedance spectroscopic (EIS) measurements were performed with a 5 mV amplitude over a frequency range from 1 000 000 to 0.1 Hz at 0 V.

Assembly of the Zn–NO_3^- battery and electrochemical tests

The Zn–NO_3^- battery was constructed using a typical H-type cell, in which the carbon cloth-supported Cu_3–Pd-PorMCOF-2 (1×1 cm^2, catalyst mass loading of 1 mg cm^{-2}) and Zn plate (2×2 cm^2) served as the cathode and anode, respectively. The catholyte (60 mL 1 M KOH + 0.1 M KNO_3) and anolyte (1 M KOH + 0.2 M $Zn(Ac)_2$) were separated by a Nafion 117 membrane. Before electrochemical tests, the catholyte was purged with high-purity Ar (99.999%) for 30 min to remove dissolved O_2. The open-circuit voltage test, discharging polarization measurements at a scan rate of 10 mV s^{-1}, and chronoamperometry (i–t) and discharge–charge measurements at a constant current density of 1 mA cm^{-2} were conducted on a CHI 660E workstation (Shanghai Chenhua) at room temperature. After electrochemical tests, the catholyte was collected and the ammonia concentration was measured through the indophenol blue method.

The power density (P) of the $Zn–NO_3^-$ battery was calculated using the following formula:

$$P = I \times V$$

where I and V are the discharge current density and voltage, respectively.

Results and discussion

Synthesis and characterization

Three new porphyrin ligands such as Pd(II)-5,15-diphenyl-10,20-bis(4-aminophenyl)porphyrin (Pd-DAPP), Pd(II)-5,15-bis(4-ethoxyphenyl)-10,20-bis(4-aminophenyl)porphyrin (Pd-EDAPP) and 5,15-bis(4-ethoxyphenyl)-10,20-bis(4-aminophenyl) porphyrin (EDAPP) were designed and synthesized (Fig. S6). The solvothermal reaction of Pd-DAPP, Pd-EDAPP and EDAPP and tris(μ_2-4-carboxaldehyde-pyrazolato-N,N')-tricopper ($Cu_3(PyCA)_3$, Fig. S7 and S8) in the presence of 6 M trifluoroacetic acid (TFA) generated three imine bonded covalent organic frameworks named as Pd-PCOF-1(Cu_3), Pd-PCOF-2(Cu_3) and PCOF-2(Cu_3), respectively (Fig. 2 and S9–S11). The three PCOFs were predicted to possess well-aligned frameworks with a hcb topology, according to the [3 + 2] ligand combination.

The crystalline architectures of Pd-PCOF-1(Cu_3), Pd-PCOF-2(Cu_3) and PCOF-2(Cu_3) were determined *via* powder X-ray diffraction (PXRD) measurement and theoretical structural simulations *via* Materials Studio (Fig. 3a–c). Pd-PCOF-1(Cu_3) exhibited two distinct peaks at $2\theta = 3.40°$ and 6.80°, corresponding to the (110) and (220) planes, respectively (Fig. 3d). Pawley refinement gave the optimized unit cell parameters of $a = b = 54.020$ Å, $c = 6.739$ Å, $\alpha = \beta = 90.00°$, $\gamma = 120.00°$, with good agreement parameters of $R_p = 3.70\%$ and $R_{wp} = 3.20\%$ for Pd-PCOF-1(Cu_3) (Tables S2–S4). According to theoretical structure simulations, the experimental PXRD patterns of Pd-PCOF-1(Cu_3) well agreed with the simulated ABC stacking (staggered) model in the R-3 space group rather than the AA or AB stacking model (Fig. S12 and S13). It is noted that the PXRD patterns of the three PCOFs were different from those of Pd-DAPP, Pd-EDAPP, EDAPP and $Cu_3(PyCA)_3$, demonstrating the formation of the new crystal structures (Fig. S14–S16).

Pd-PCOF-2(Cu_3) and PCOF-2(Cu_3) displayed similar PXRD patterns and sharper diffraction peaks than Pd-PCOF-1(Cu_3), indicating that the introduction of the ethyl group significantly improved crystallinity but did not fundamentally alter the structure of the ABC stacking model in the R-3 space group (Fig. 3e, f, S17–S20 and Tables S5–S10). Taking Pd-PCOF-2(Cu_3) as an example, the PXRD pattern of Pd-PCOF-2(Cu_3) displayed

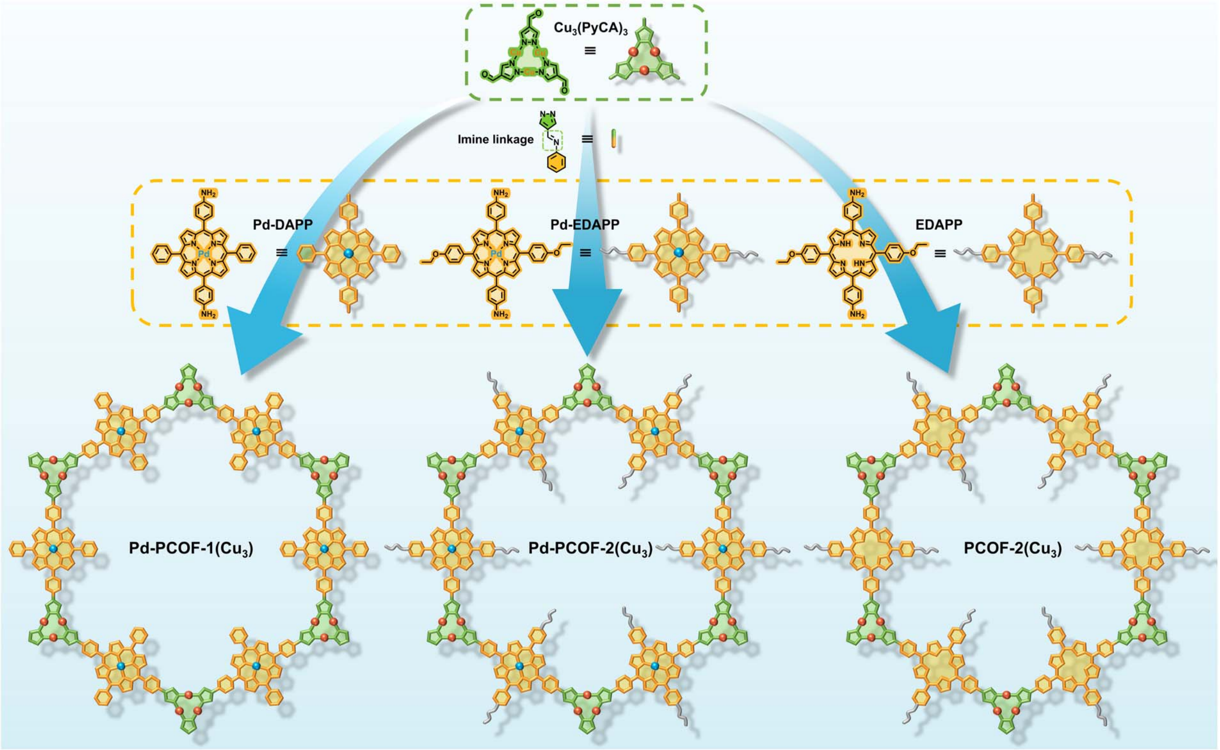

Fig. 2 Synthesis of Pd-PCOF-1(Cu_3), Pd-PCOF-2(Cu_3) and PCOF-2(Cu_3).

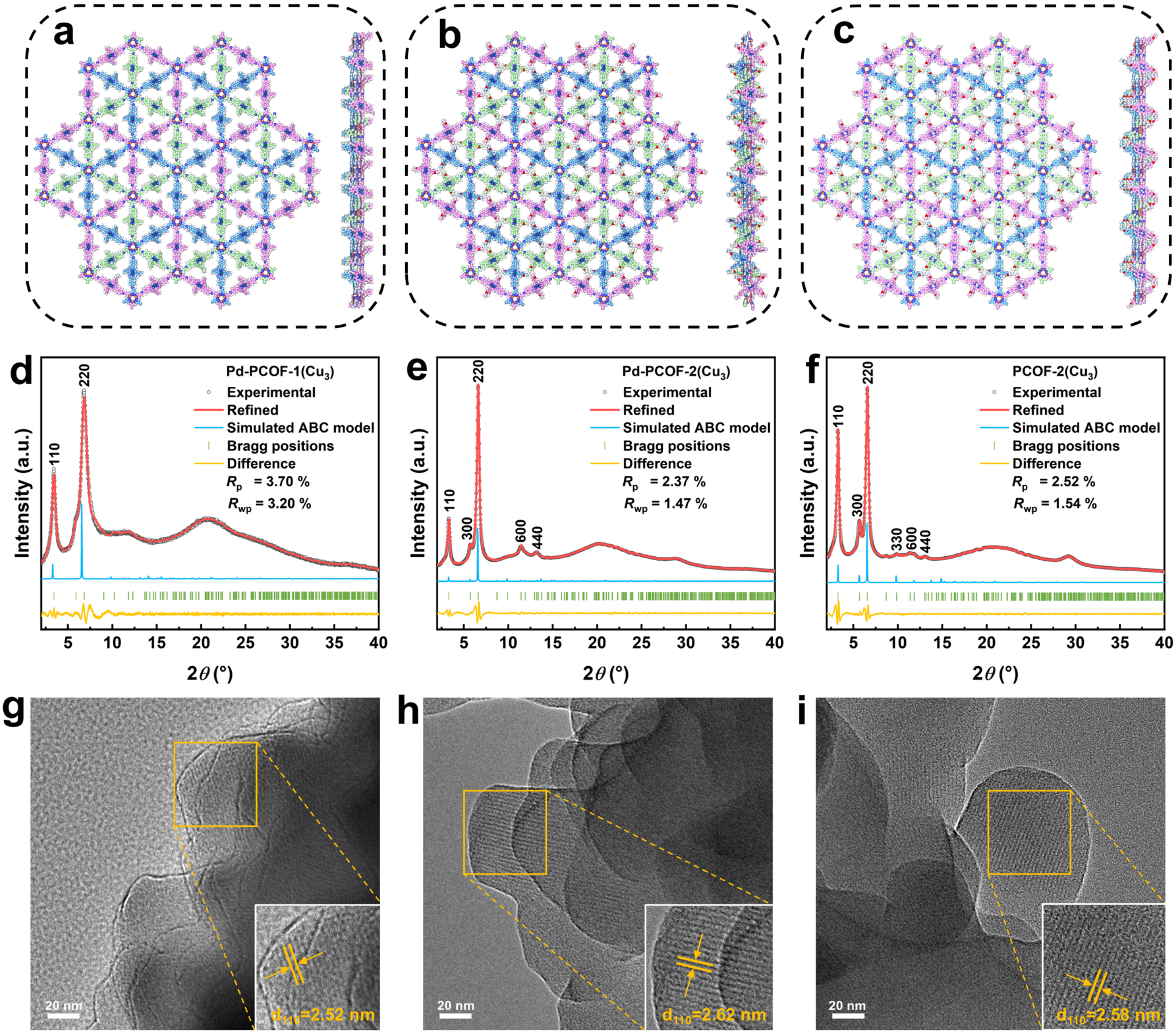

Fig. 3 ABC stacking model of Pd-PCOF-1(Cu_3) (a), Pd-PCOF-2(Cu_3) (b) and PCOF-2(Cu_3) (c) viewed from the *c* axis (left) and *a* axis (right). PXRD patterns of Pd-PCOF-1(Cu_3) (d), Pd-PCOF-2(Cu_3) (e) and PCOF-2(Cu_3) (f), showing the experimental profiles, Pawley refinement fits, difference curves, and simulated profiles based on ABC models. HR-TEM images of Pd-PCOF-1(Cu_3) (g), Pd-PCOF-2(Cu_3) (h) and PCOF-2(Cu_3) (i), and the insets are enlarged images of a selective area showing a well-ordered lattice fringe of (110).

two dominant peaks at $2\theta = 3.30°$ and $6.60°$ and three weaker peaks at $2\theta = 5.76°$, $11.44°$ and $13.20°$, which were assigned to the (110), (220), (300), (600), and (440) facet diffractions in the calculated ABC stacking mode, respectively (Fig. 3e, S17 and S18). The simulated PXRD curve of the ABC stacking model matched well with the experimental one with small fitting parameters of $R_p = 2.37\%$ and $R_{wp} = 1.47\%$ and the optimized unit cell parameters were determined to be $a = b = 53.903$ Å, $c = 6.953$ Å, $\alpha = \beta = 90.00°$ and $\gamma = 120.00°$ on the basis of the Pawley refinement (Table S7).

A scanning electron microscope (SEM) and high-resolution transmission electron microscope (HR-TEM) were used to investigate the morphology and crystal structure of these three PCOFs. In the SEM images, the three PCOFs exhibited irregular nanoparticles with sizes ranging from 100 to 200 nm (Fig. S21–S23). Their HR-TEM images displayed distinct lattice fringes with a spacing of approximately 2.52, 2.62 and 2.58 nm for Pd-PCOF-1(Cu_3), Pd-PCOF-2(Cu_3) and PCOF-2(Cu_3), respectively, corresponding to their (110) facets, which were in good agreement with the theoretical values of 27.02, 26.95 and 27.06 Å based on the ABC stacking model, further proving their high crystallinity (Fig. 3g–i).

Fourier transform infrared (FT-IR) spectrometry was employed to analyze the chemical structure of the three PCOFs (Fig. 4a). The peak of the C=O stretching vibration of Cu_3(PyCA)$_3$ appeared at 1670 cm^{-1}, and meanwhile, the N–H and C=N stretching vibrations of the porphyrin rings were located at 3300–3500 and 1620 cm^{-1}, respectively (Fig. S24–S26).

N_2 adsorption–desorption isotherms at 77 K were employed to characterize the porosity of Pd-PCOF-1(Cu_3), Pd-PCOF-2(Cu_3)

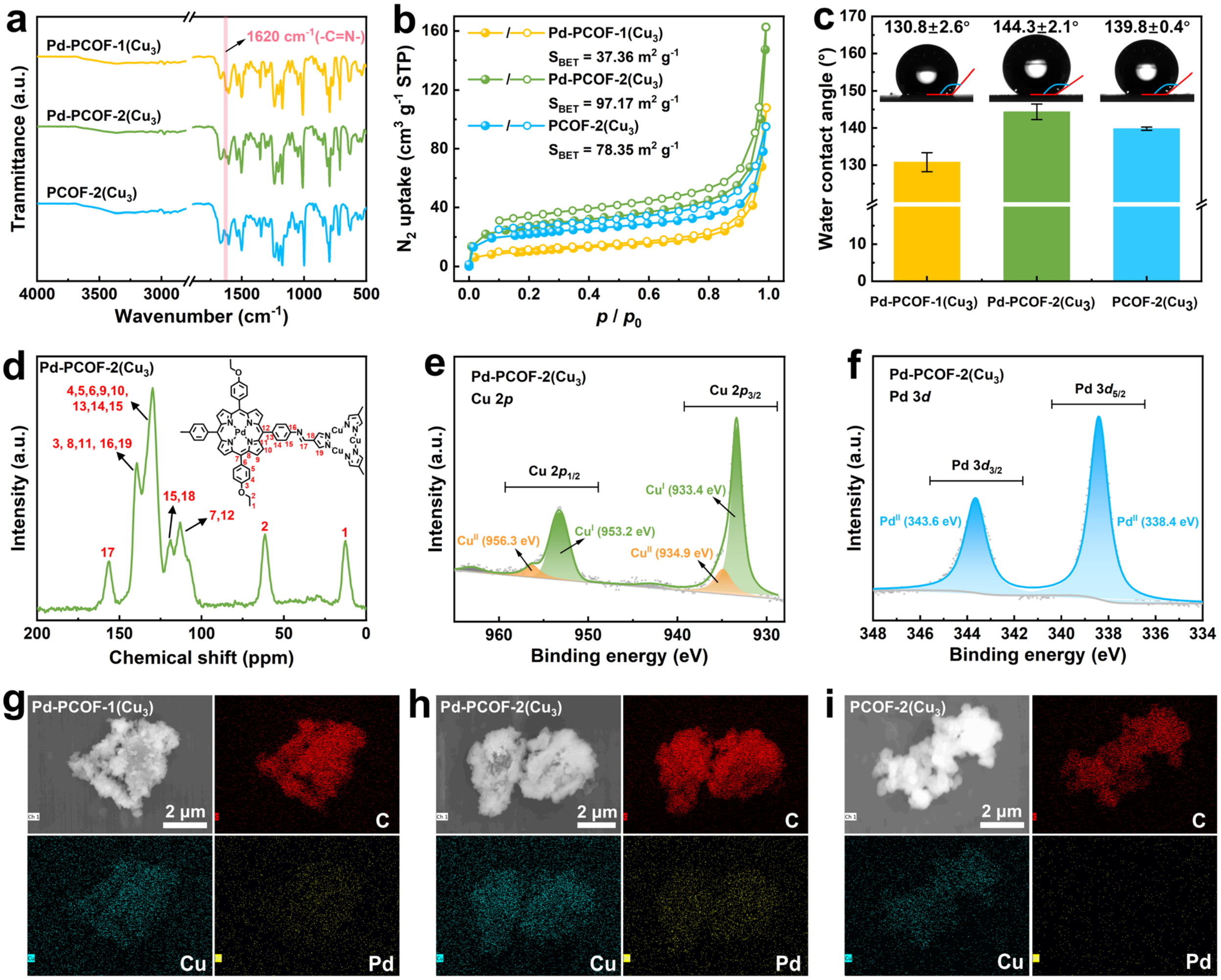

Fig. 4 FT-IR spectra (a), N_2 adsorption isotherm curve profiles (b) and water contact angles (c) of PCOFs. Solid-state ^{13}C CP-MAS NMR spectra (d) and XPS spectra of Cu 2p (e) and Pd 3d (f) for Pd-PCOF-2(Cu_3). EDS elemental mapping of PCOF (g–i).

and PCOF-2(Cu_3) (Fig. 4b). All three COFs exhibited typical type-II reversible isotherms with Brunauer–Emmett–Teller (BET) surface areas of 37.36, 97.17 and 78.15 m^2 g^{-1} for Pd-PCOF-1(Cu_3), Pd-PCOF-2(Cu_3) and PCOF-2(Cu_3), respectively. The reduced BET surface area of Pd-PCOF-1(Cu_3) may be attributed to its lower crystallinity than Pd-PCOF-2(Cu_3) and PCOF-2(Cu_3). According to the nonlocal density functional theory (NLDFT) method, the pore sizes were predominantly distributed at approximately 0.93, 0.80, and 0.88 nm for Pd-PCOF-1(Cu_3), Pd-PCOF-2(Cu_3) and PCOF-2(Cu_3), respectively (Fig. S27).

According to the static water contact angle measurement, obvious hydrophobicity was visualized in the three PCOFs, in which the water contact angles were measured to be 130.8°, 144.3° and 139.8° for Pd-PCOF-1(Cu_3), Pd-PCOF-2(Cu_3) and PCOF-2(Cu_3), respectively (Fig. 4c). Compared with Pd-PCOF-1(Cu_3), the increased water contact angles of Pd-PCOF-2(Cu_3) and PCOF-2(Cu_3) might be attributed to the presence of ethoxyphenyl groups within the channels.

The solid-state ^{13}C cross-polarization magic angle spinning nuclear magnetic resonance (^{13}C CP-MAS NMR) spectrum of Pd-PCOF-2(Cu_3) was examined. The characteristic C signal of the ethoxy group was observed at 61.5 and 12.5 ppm, while the porphyrin ring and pyrazole carbons exhibited resonance at 139.5, 129.5, 118.5 and 113.0 ppm and 139.5 and 118.5 ppm, respectively, in Pd-PCOF-2(Cu_3) (Fig. 4d). The characteristic resonance peak of the imine carbon appeared at ~156.5 ppm in the ^{13}C CP-MAS NMR spectrum, which further confirmed the successful formation of imine bonds.

The electronic valence state of the PCOFs was investigated by X-ray photoelectron spectroscopy (XPS) measurements. The full XPS spectra of both Pd-PCOF-1(Cu_3) and Pd-PCOF-2(Cu_3) displayed C 1s, N 1s, O1s, Cu 2p and Pd 3d elemental signal peaks, while the full XPS spectrum of PCOF-2(Cu_3) only showed C 1s, N 1s, O1s and Cu 2p elemental signal peaks (Fig. S28). Furthermore, the high-resolution Cu 2p XPS spectrum of Pd-PCOF-2(Cu_3) showed two major peaks belonging to Cu $2p_{1/2}$ and Cu $2p_{3/2}$, which were mainly composed of peaks assigned to the binding energy of Cu^I centered at 953.2 and 933.4 eV (Fig. 4e). Similar values were observed for Pd-PCOF-1(Cu_3) (953.2 and 933.4 eV), PCOF-2(Cu_3) (953.1 and 933.2 eV) and $Cu_3(PyCA)_3$ (952.8 and 933.0 eV), revealing the main Cu^I state nature of the Cu_3 moiety (Fig. S29). The high-resolution Pd 3*d* XPS spectrum of Pd-EDAPP, Pd-PCOF-1(Cu_3) and Pd-PCOF-2(Cu_3) all exhibited two peaks centered at 343.6 and 338.4 eV, corresponding to Pd $3d_{3/2}$ and Pd $3d_{5/2}$, respectively, indicating a +2 oxidation state of the coordinated palladium centers in porphyrin (Fig. 4f and S30). The results of XPS spectra demonstrated that the formation of PCOFs did not alter the oxidation states of copper and palladium of the starting materials.

Energy-dispersive X-ray (EDS) spectroscopy was employed to investigate elemental distribution, revealing the homogeneous dispersion of C, Cu and Pd in both Pd-PCOF-1(Cu_3) and Pd-PCOF-2(Cu_3), whilst only C and Cu were observed in PCOF-2(Cu_3) (Fig. 4g–i).

The chemical structural stability of the PCOFs was first studied by thermogravimetric analysis (TGA), which disclosed only 5% mass loss at 265, 244 and 235 °C under a N_2 atmosphere for Pd-PCOF-1(Cu_3), Pd-PCOF-2(Cu_3) and PCOF-2(Cu_3), respectively (Fig. S31). Furthermore, the PXRD patterns of Pd-PCOF-2(Cu_3) and PCOF-2(Cu_3) remained almost unchanged after being soaked in a range of solvents such as tetrahydrofuran (THF), acetonitrile (CH_3CN), methanol (CH_3OH), 1 M NaOH and 0.1 M HCl for 24 h (Fig. S32 and S33). Pd-PCOF-1(Cu_3) was also stable in these solvents with the exception of 0.1 M HCl (Fig. S34). These studies revealed the high chemical structural stability of these PCOFs and the importance of hydrophobicity in their acid-base resistance.

Electrocatalytic performances

Electrocatalytic NO_3RR performances of Pd-PCOF-1(Cu_3), Pd-PCOF-2(Cu_3) and PCOF-2(Cu_3) were evaluated in a standard three-electrode H-type cell containing 1 M KOH with 0.1 M KNO_3 at room temperature (Fig. S35). All potentials were referenced against the RHE without *iR* compensation. ^1H NMR measurement and ultraviolet-visible (UV-vis) spectrophotometry based on the indophenol blue method were employed to quantify NH_3, while UV-vis spectrophotometry based on the Griess test and gas chromatography were used to detect NO_2^-

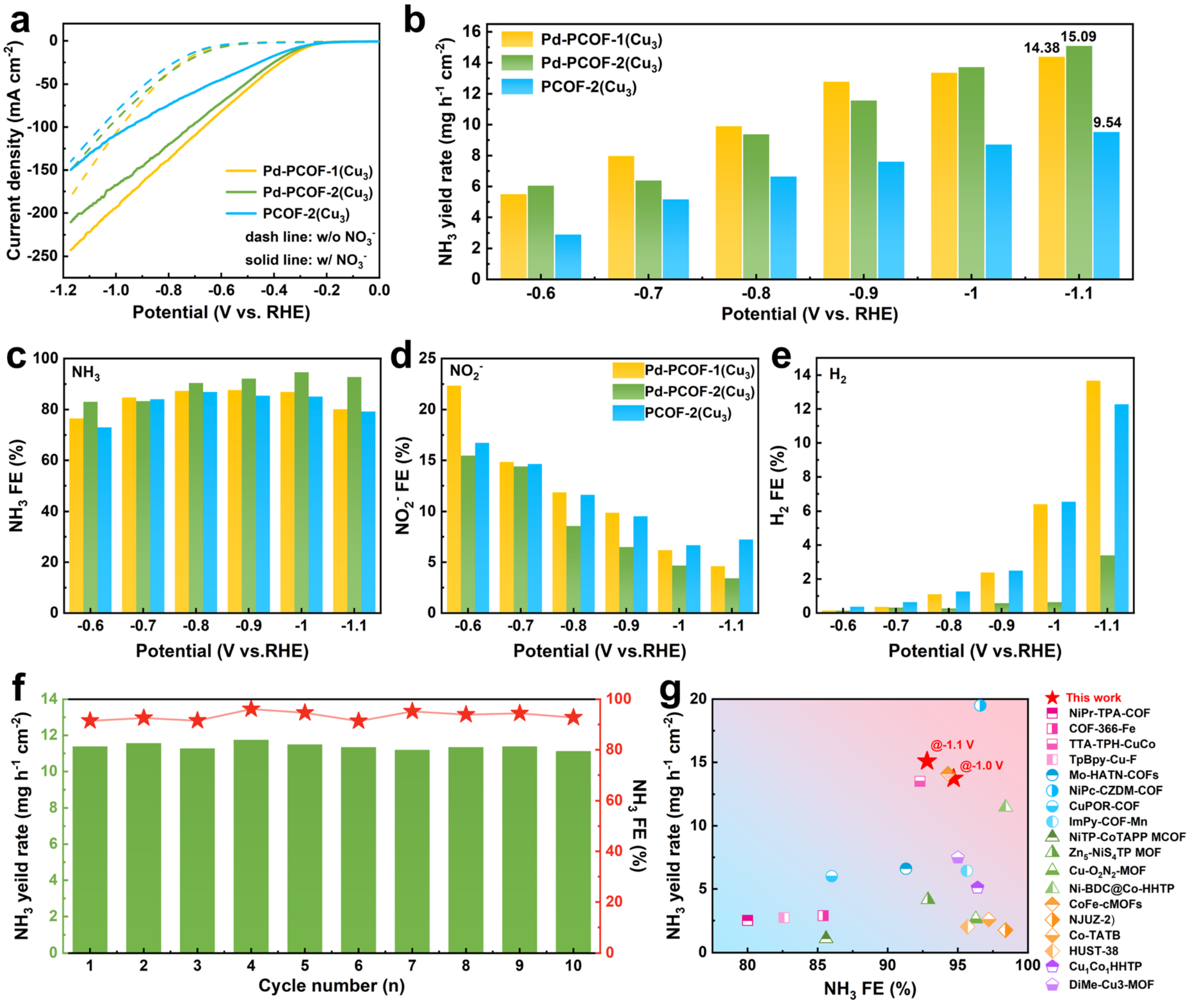

Fig. 5 Linear scanning voltammetry (LSV) curves of Pd-PCOF-1(Cu_3), Pd-PCOF-2(Cu_3) and PCOF-2(Cu_3) in 1 M KOH with 0.1 M KNO_3 (solid lines) or without KNO_3 (dash lines) at a scan rate of 10 mV s^{-1} (a). NH_3 yield rate of Pd-PCOF-1(Cu_3), Pd-PCOF-2(Cu_3) and PCOF-2(Cu_3) at different applied potentials (b). NH_3 (c), NO_2^- (d) and H_2 (e) FEs of Pd-PCOF-1(Cu_3), Pd-PCOF-2(Cu_3) and PCOF-2(Cu_3) at different applied potentials. Stability of Pd-PCOF-2(Cu_3) for NO_3RR at −0.9 V *vs.* RHE (f). Comparison of NH_3 yield rate and FE of Pd-PCOF-2(Cu_3) with reported MOF/COF-based electrocatalysts (Table S1) (g).

and H_2, respectively. The corresponding calibration curves are presented in Fig. S36–S39.

The linear sweep voltammetry (LSV) curves revealed a dramatic enhancement in the current density upon the addition of NO_3^- for the three PCOFs, manifesting their remarkable electrocatalytic NO_3RR activity (Fig. 5a). Pd-PCOF-1(Cu_3) and Pd-PCOF-2(Cu_3) displayed stronger current density responses than PCOF-2(Cu_3), suggesting that the incorporation of Pd centers in porphyrin could improve the NO_3RR activity.

Chronoamperometry electrolysis with applied potentials from −0.6 to −1.1 V *vs.* RHE was employed to investigate the differences in electrocatalytic efficiency among Pd-PCOF-1(Cu_3), Pd-PCOF-2(Cu_3) and PCOF-2(Cu_3) (Fig. S40–S42). The NH_3 generation rate exhibited a nearly linear enhance with increasingly negative applied potential and reached the maximum values of 14.34 and 15.09 mg h^{-1} cm^{-2} at −1.1 V *vs.* RHE for Pd-PCOF-1(Cu_3) and Pd-PCOF-2(Cu_3), respectively, which were superior to that of PCOF-2(Cu_3) (9.52 mg h^{-1} cm^{-2}), further demonstrating the contribution of the Pd center in porphyrin to enhance the overall electrocatalytic activity (Fig. 5b). The faradaic efficiencies (FEs) of NH_3 exhibited a typical volcano-shaped trend (Fig. 5c). Pd-PCOF-2(Cu_3) maintained the highest NH_3 FEs (over 80%) among the three PCOFs at almost all applied potentials and reached the maximum value of 94.70% at −1.0 V *vs.* RHE, which was significantly higher than those of Pd-PCOF-1(Cu_3) (87.69% at −0.9 V *vs.* RHE) and PCOF-2(Cu_3) (86.96% at −0.8 V *vs.* RHE).

The NO_2^- FEs of all the PCOFs gradually decreased with increasingly negative potentials, under which conditions more active hydrogen (H*) could be generated, which subsequently promoted the hydrogenation of NO_2^- to NH_3, thereby reducing the accumulation of NO_2^- (Fig. 5d). For comparison, the H_2 FEs increased sharply with increasingly negative potentials (Fig. 5e). Compared to Pd-PCOF-1(Cu_3) and PCOF-2(Cu_3), Pd-PCOF-2(Cu_3) exhibited much lower H_2 FEs at all potentials. This demonstrated that the hydrophobic microenvironment suppressed the HER, while the generation of H* at Pd-porphyrin promoted the NO_3RR process .

Pd-PCOF-2(Cu_3) maintained excellent electrocatalytic performance stability for NO_3RR at −0.9 V *vs.* RHE over 10 consecutive cycles, without obvious degradation in FE and the generation rate of NH_3 (Fig. 5f and S43). The PXRD pattern of Pd-PCOF-2(Cu_3)

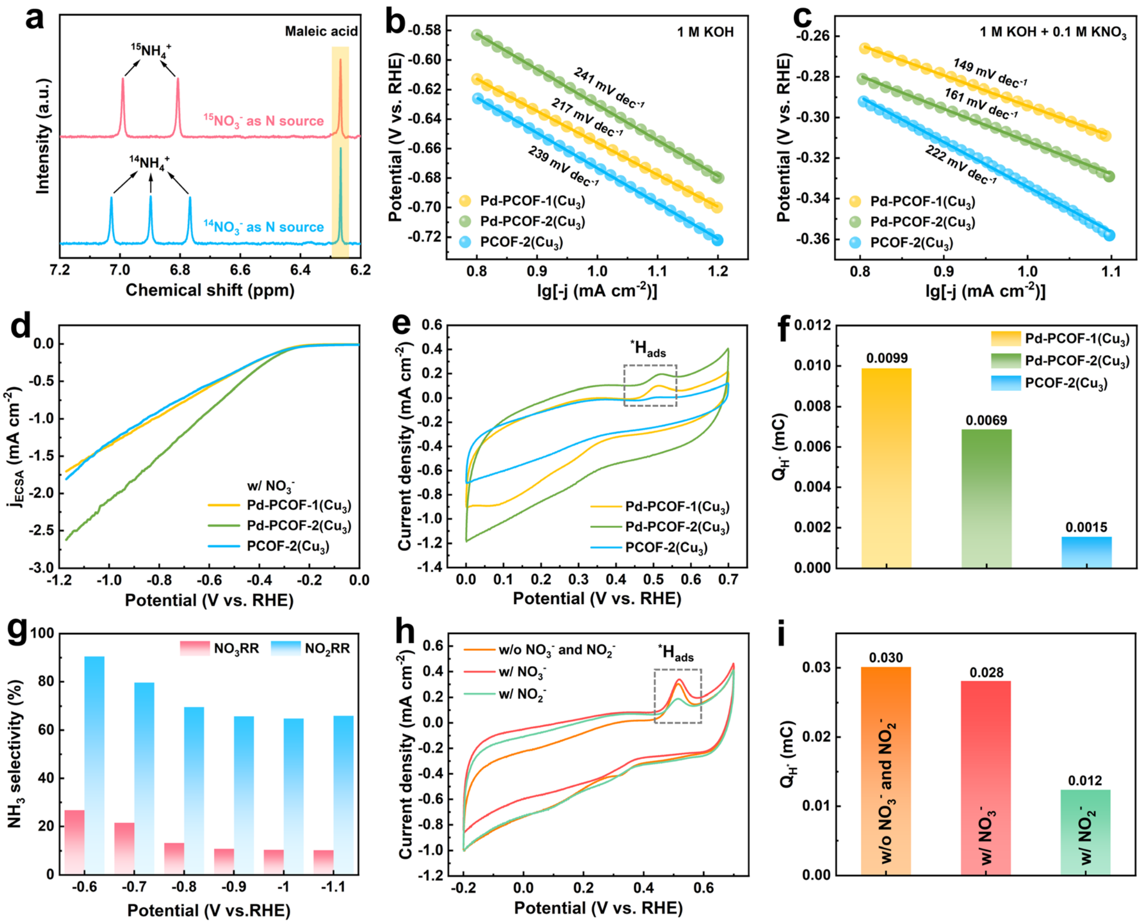

Fig. 6 ^1H NMR spectra of the electrolytes employing $^{14}NO_3^-$ or $^{15}NO_3^-$ as the N source over Pd-PCOF-2(Cu_3) (a). The Tafel plots in 1 M KOH electrolyte (b) and 1 M KOH containing 0.1 M KNO_3 electrolyte (c) of Pd-PCOF-1(Cu_3), Pd-PCOF-2(Cu_3) and PCOF-2(Cu_3). LSV curves normalized by ECSA (d). CV curves (e) and the corresponding charges of $^*H_{ads}$ (Q_{H^*}) (f) of Pd-PCOF-1(Cu_3), Pd-PCOF-2(Cu_3) and PCOF-2(Cu_3) in 1 M KOH. NH_3 selectivity of Pd-EDAPP for NO_3RR and NO_2RR at different applied potentials (g). CV curves (h) and the corresponding charges of $^*H_{ads}$ (Q_{H^*}) (i) of Pd-EDAPP in 1 M KOH and containing 0.1 M KNO_3 or 0.1 M KNO_2.

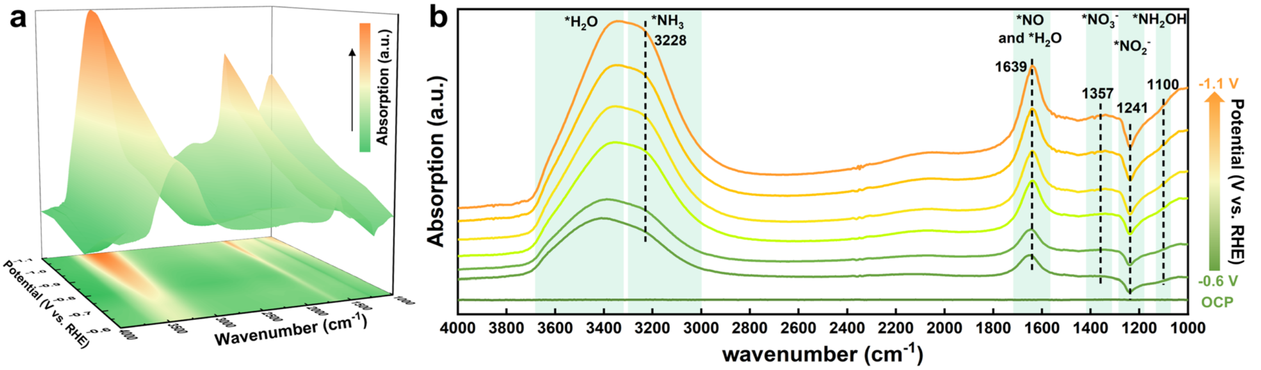

Fig. 7 The 3D *in situ* ATR-FTIR colormap surface with projection of Pd-PCOF-2(Cu_3) for NO_3RR (a). Electrochemical *in situ* ATR-FTIR spectra of Pd-PCOF-2(Cu_3) for NO_3RR at different applied potentials (b).

after electrocatalysis over 10 consecutive cycles retained characteristic diffraction peaks at $2\theta = 3.30°$ and $6.60°$ (Fig. S44).

In short, owing to the suppression of the competitive HER by the hydrophobic microenvironment and the synergistic catalysis of the Cu_3 cluster and Pd-porphyrin, Pd-PCOF-2(Cu_3) achieved superior electrocatalytic performances for NO_3RR in terms of NH_3 FE and generation rate in comparison with most reported MOF/COF-based electrocatalysts (Fig. 5g and Table S1).

Reaction mechanism studies

To gain a more in-depth and comprehensive understanding of the reaction mechanism of NO_3RR, further investigations were carried out. First, ^{15}N isotopic labeling experiments were performed to identify the origin of nitrogen in the NH_3 produced. The ^1H NMR spectra of the electrolytes employing $^{14}NO_3^-$ and $^{15}NO_3^-$ as N sources revealed the typical characteristic triplet peaks of $^{14}NH_4^+$ (at 6.77, 6.90 and 7.03 ppm) and doublet peaks of $^{15}NH_4^+$ (at 6.81 and 6.99 ppm), respectively, confirming that NH_3 originated from the electrocatalytic NO_3RR (Fig. 6a and S45).

Pd-PCOF-2(Cu_3) (241 mV dec^{-1}) and PCOF-2(Cu_3) (239 mV dec^{-1}) manifested higher Tafel slopes than Pd-PCOF-1(Cu_3) (217 mV dec^{-1}), revealing an inhibitory effect of the hydrophobic microenvironment on the water dissociation kinetics (Fig. 6b). It is noted that the H* generated from water dissociation ($H_2O + M + e^- \rightarrow M{-}H^* + OH^-$) is crucial to the deoxygenation and hydrogenation of NO_3^- and intermediates. With the addition of NO_3^-, Tafel slopes of Pd-PCOF-1(Cu_3) and Pd-PCOF-2(Cu_3) decreased significantly to 149 and 161 mV dec^{-1}, respectively, which were lower than that of PCOF-2(Cu_3) (222 mV dec^{-1}), demonstrating that the presence of Pd centers in the porphyrin rings enhanced NO_3RR kinetics (Fig. 6c). In addition, Pd-porphyrin-based COFs of Pd-PCOF-1(Cu_3) (2.4 Ω) and Pd-PCOF-2(Cu_3) (2.8 Ω) exhibited lower charge transfer resistance than PCOF-2(Cu_3) (3.1 Ω) (Fig. S46).

According to LSV curves normalized by electrochemical surface area (ECSA, Fig. S47), Pd-PCOF-2(Cu_3) presented a higher current density response than Pd-PCOF-1(Cu_3) and PCOF-2(Cu_3), demonstrating the highest intrinsic NO_3RR activity of Pd-PCOF-2(Cu_3) (Fig. 6d).

Cyclic voltammogram (CV) curves revealed that the peaks located at 0.52 V *vs.* RHE in the anodic scan were attributed to adsorbed active hydrogen (*H_{ads}) (Fig. 6e), which could be magnified for precise integration (Fig. S48). The ability to generate *H could be quantitatively compared based on the charge required to oxidize these H* (Q_{H^*}). Pd-PCOF-1(Cu_3) and Pd-PCOF-2(Cu_3) exhibited Q_{H^*} values of 0.0099 and 0.0069 mC, respectively, which were higher than that of PCOF-2(Cu_3) (0.0015 mC), indicative of the stronger H* supply ability of Pd-porphyrin-based COFs (Fig. 6f).

To investigate the synergistic effect of the Cu_3-cluster and Pd-porphyrin within Pd-PCOF-2(Cu_3), electrocatalytic NO_3RR performances of $Cu_3(PyCA)_3$ and Pd-EDAPP were evaluated under similar conditions. $Cu_3(PyCA)_3$ showed much higher current density and NH_3 FEs than Pd-EDAPP, suggesting that $Cu_3(PyCA)_3$ was the main active center for NO_3RR (Fig. S49 and S50). $Cu_3(PyCA)_3$ displayed high NH_3 FEs (65.0∼84.4%) from −0.6 to 1.1 V (*vs.* RHE) but negligible H_2 FEs at −0.6 V (*vs.* RHE). With increasingly negative potentials, the H_2 FE increased up to 26.6% at −1.1 V (*vs.* RHE), indicating that it was difficult for Cu_3

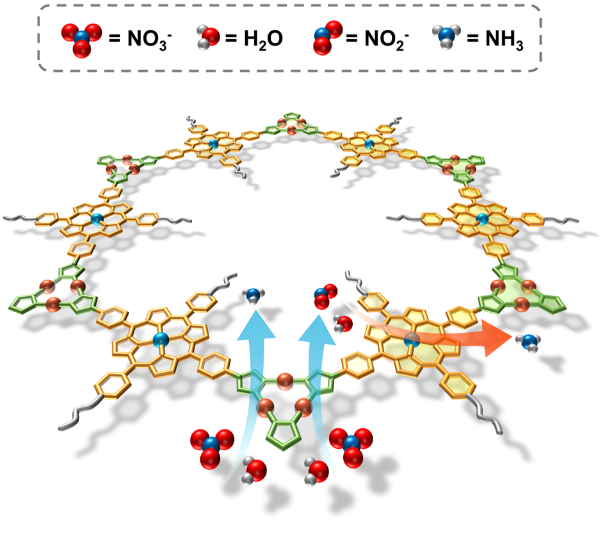

Fig. 8 Schematic illustration of the catalytic mechanism for NO_3RR over Pd-PCOF-2(Cu_3).

to achieve precise kinetic matching between the generation of H* and the deoxygenation process of NO_3^- (Fig. S49d). For comparison, Pd-EDAPP displayed low NH_3 FEs but high H_2 FEs (56.2∼84.5%) at all potentials, suggesting that the Pd center in porphyrin exhibited slow kinetics for the NO_3^- activation, giving rise to H_2 *via* the self-coupling of H* as the only rapid outlet (Fig. S50e). Moreover, both $Cu_3(PyCA)_3$ and Pd-EDAPP exhibited high performance in the NO_2RR process, and the NH_3 FEs remained consistently above 60% across the entire applied potential window (Fig. S51 and S52).

Catalytic results further showed that Pd-EDAPP could much more effectively activate NO_2^- than NO_3^- (Fig. 6g and S53). A comparison of the LSV curves for catalytic NO_2RR demonstrated that the current density of Pd-EDAPP became much higher than that of $Cu_3(PyCA)_3$ with increasingly negative applied potential (Fig. S54a). Meanwhile, the NH_3 yield rate of Pd-EDAPP was much higher than that of $Cu_3(PyCA)_3$ in NO_2RR (Fig. S54b). Comparison of the consumption rate of H* on NO_2RR and NO_3RR showed that the H* generated at Pd-porphyrin showed a stronger affinity for NO_2^- than NO_3^- (Fig. 6h, i and S55). These results demonstrated that during electrocatalytic nitrate reduction, Cu_3 primarily activated NO_3^- and converted a portion of NO_2^- to NH_3, while Pd-porphyrin played a synergistic role in promoting the conversion of NO_2^- to NH_3.

To uncover the detailed reaction pathway of NO_3RR, *in situ* electrochemical ATR-FTIR spectroscopy was employed under applied potentials ranging from −0.6 to −1.1 V *vs.* RHE to identify reaction intermediates, which were generated on the surface of the Pd-PCOF-2(Cu_3) catalyst. The 3D *in situ* ATR-FTIR colormap spectra revealed distinct distributions of absorption peaks at various applied potentials (Fig. 7a). The intensity of these peaks gradually increased as the applied potential became more negative. The *in situ* ATR-FTIR spectra were scrutinized over the wavenumber interval of 4000–1000 cm^{-1}, and the upward and downward bands corresponded to the formation of various nitrogen intermediates and the consumption of the corresponding reactants, respectively (Fig. 7b). The pronounced absorption peaks at around 3400 and 3228 cm^{-1} were attributed to the O–H stretching of $*H_2O$ and the N–H stretching of NH_3, respectively.[38] The intensity of these peaks augmented as the

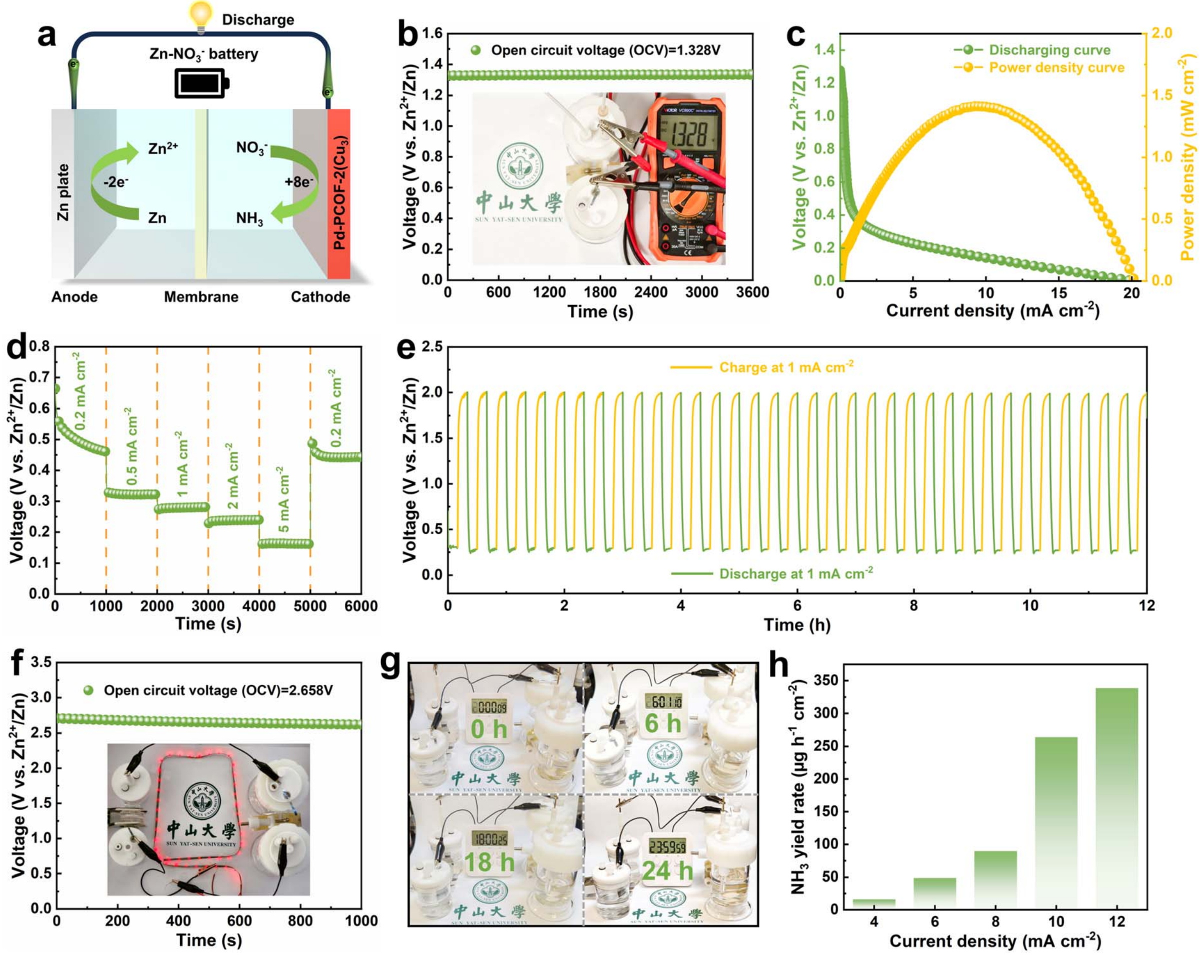

Fig. 9 Schematic illustration of the $Zn–NO_3^-$ battery with a Pd-PCOF-2(Cu_3) cathode (a). Open-circuit voltage (OCV) of the Pd-PCOF-2(Cu_3) based $Zn–NO_3^-$ battery (b). Polarization curve for the $Zn–NO_3^-$ battery and the resultant power density (c). Galvanostatic discharge curves at different current densities (d). Charge–discharge cycling curves of the $Zn–NO_3^-$ battery at 1 mA cm^{-2} (e). Open-circuit voltage (OCV) of two $Zn–NO_3^-$ batteries in series (f). Photographs of LED light strips (inside f) and electronic timer (g) powered by $Zn–NO_3^-$ batteries. NH_3 yield rate derived from the $Zn–NO_3^-$ battery at different discharge current densities (h).

potential decreased from −0.6 to −1.1 V *vs.* RHE, indicative of the increase in NH_3 production rate and an enhanced H_2O molecule adsorption and dissociation process. Within the 2000–1000 cm^{-1} wavenumber domain, the absorption peak at 1639 cm^{-1} was attributed to $*NO$ and $*H_2O$.[39] The weak but discernible absorption bands at 1357 and 1100 cm^{-1} were assigned to the N–O asymmetric stretching of $*NO_3$ and $*NH_2OH$, respectively.[40] Moreover, the downward band at 1241 cm^{-1} was ascribed to the N–O antisymmetric stretching of $*NO_2$ and exhibited intensified strengths at more negative potentials.[41]

Based on the above mechanistic studies and *in situ* ATR-FTIR spectra analysis, a reaction pathway for the NO_3RR over Pd-PCOF-2(Cu_3) might be deduced: $NO_3^- \rightarrow *NO_3 \rightarrow *NO_2 \rightarrow *NO \rightarrow *NH_2OH \rightarrow *NH_3 \rightarrow NH_3$. Consequently, NO_2^- was a critical intermediate and its excessive accumulation could lower the reaction selectivity and efficiency. The H* generated at the catalytic sites could promote the hydrogenation of NO_2^-, but its oversupply could also facilitate the competitive HER, thereby degrading the selectivity of NO_3RR. Therefore, the precise modulation of the conversion rate of NO_2^- and the supply rate of H* was crucial for enhancing both the reaction rate and the selectivity toward NH_3. In Pd-PCOF-2(Cu_3)-catalyzed NO_3RR, Cu_3 served as the primary active sites for the initial deoxygenation of NO_3^- to the NO_2^- intermediate. Subsequently, Cu_3 partially hydrogenated NO_2^- to NH_3 while the unconverted NO_2^- migrated to the Pd-porphyrin for subsequent hydrogenation, which could not only effectively mitigate the accumulation of the detrimental NO_2^- intermediate but also accelerate the overall NO_3^- to NH_3 conversion kinetics. Furthermore, the tailored hydrophobic microenvironment could enable precise modulation of the H* supply for expediting the NO_2^- hydrogenation rather than the HER. In short, an accelerated catalytic mechanism *via* synergistic tandem of bimetallic site and modulation of the hydrophobic microenvironment was elucidated (Fig. 8).

Zn–NO_3^- battery

Inspired by the NO_3RR performances of Pd-PCOF-2(Cu_3), a rechargeable Zn–NO_3^- battery was constructed, which could not only generate electricity but also synthesize value-added NH_3 from NO_3^-. The Zn–NO_3^- battery was assembled with Pd-PCOF-2(Cu_3) as the cathode and a Zn plate as the anode (Fig. 9a). The assembled Zn–NO_3^- battery exhibited a high and stable open-circuit voltage (OCV) of approximately 1.328 V *vs.* Zn^{2+}/Zn for up to 3600 s (Fig. 9b). The battery exhibited a maximum power density of 1.41 mW cm^{-2} at a current density of 9.62 mA cm^{-2} and a stable discharge profile over a wide range of current densities from 0.2 to 5 mA cm^{-2} (Fig. 9c and d). It also maintained a stable voltage output over 12 h during continuous discharge–charge cycling at a current density of 1 mA cm^{-2} (Fig. 9e). To verify the practical applicability of the battery, two series-connected batteries were assembled, which achieved a high OCV of approximately 2.658 V *vs.* Zn^{2+}/Zn. The system successfully lit a Light Emitting Diode (LED) strip or powered a commercial electronic timer (usually driven by a commercial 1.5 V dry battery) for 24 h (Fig. 9f and g). NH_3 production was quantitatively analyzed after discharge under current densities of 4, 6, 8, 10 and 12 mA cm^{-2}, showing that the NH_3 generation rate increased with current density, reaching the highest value of 338.6 μg h^{-1} cm^{-2} (Fig. 9h and S56). These results emphasized the great potential of the Pd-PCOF-2(Cu_3)-based Zn–NO_3^- battery as a stable multi-function platform in both power generation and NO_3^- conversion.

Conclusion

In summary, an effective molecular engineering strategy was developed to construct hydrophobic bimetallic porphyrin-based COFs, integrating Pd-porphyrin and Cu_3 within the frameworks. The prepared PCOFs achieved high NO_3RR performances in alkaline electrolytes, with the faradaic efficiency and NH_3 yield up to 94.7% and 15.09 mg h^{-1} cm^{-2}, respectively. A synergistic reaction mechanism was elucidated: Cu_3 sites primarily facilitated NO_3^- adsorption and activation to NO_2^- and then to NH_3, while adjacent Pd sites assisted in the hydrogenation of NO_2^- to NH_3, minimizing intermediate accumulation and accelerating the overall kinetics. The pore-confined hydrophobic microenvironment played a critical role in precisely regulating the H* supply, thereby suppressing the competing HER. Overall, this work designed advanced electrocatalysts through the synergistic integration of molecular-scale hydrophobicity tuning and atomic-scale bimetallic site engineering. Further work on the synthesis of porphyrin-based COFs and their catalytic applications is in progress.

Author contributions

L. Z. conceived the idea for the project and assisted with funding acquisition. F. L. conducted the investigation, experiments, and data analysis and wrote the original draft. H. L. provided assistance in the synthesis of the porphyrin ligand. C. C participated in the data analysis. L. T provided resources. D. W provided assistance in the electrocatalytic NO_3RR. C. Z provided the Materials Studio. C. S assisted with funding acquisition.

Conflicts of interest

The authors declare no competing financial interest.

Data availability

The authors confirm that the data supporting the findings of this study are available within the article and its supplementary materials (SI). Supplementary information: general information, comparison of electrocatalytic NO_3RR performances of different materials, synthesis and charaterization of PCOFs and electrocatalytic performances. See DOI: https://doi.org/10.1039/d6sc01645f.

Acknowledgements

The authors acknowledge support from the National Natural Science Foundation of China (22371306, 21821003 and

92461302) and Guangdong Basic and Applied Basic Research Foundation (2019B151502017).

References

1 X. Fu, H. Guo, D. Si, H. Zhu, Y. Lan, Y. Huang and R. Cao, *Chem. Sci.*, 2025, **16**, 13503.
2 G. Wu, W. Zhang, R. Yu, Y. Yang, J. Jiang, M. Sun, A. Du, W. He, L. Dai, X. Mao, Z. Chen and Q. Qin, *Angew. Chem., Int. Ed.*, 2024, **63**, e202410251.
3 H. Lin, J. Wei, Y. Guo, Y. Li, X. Lu, C. Zhou, S. Liu and Y.-Y. Li, *Adv. Funct. Mater.*, 2024, 2409696.
4 V. Kyriakou, I. Garagounis, A. Vourros, E. Vasileiou and M. Stoukides, *Joule*, 2020, **4**, 142–158.
5 C. Guo, J. Ran, A. Vasileff and S.-Z. Qiao, *Energy Environ. Sci.*, 2018, **11**, 45.
6 D. Liu, L. Qiao, S. Peng, H. Bai, C. Liu, W. F. Ip, K. H. Lo, H. Liu, K. W. Ng, S. Wang, X. Yang and H. Pan, *Adv. Funct. Mater.*, 2023, **33**, 2303480.
7 W. Zhong, Z. Gong, P. Chen, Q. Cao, X. Liu, Y. Chen and Z. Lin, *Chem Catal.*, 2025, **4**, 101060.
8 Q. Tian, X. Ye, L. Jing, W. Wang, Z. Zheng, A. Li, K. Xie, X. Huang, Q. Hu, H. Yang, X. Zhang and C. He, *Angew. Chem., Int. Ed.*, 2025, e202516919.
9 X. Zhang, X. Liu, Z.-F. Huang, L. Gan, S. Zhang, R. Jia, M. Ajmal, L. Pan, C. Shi, X. Zhang, G. Yang and J.-J. Zou, *Energy Environ. Sci.*, 2024, **17**, 6717–6727.
10 S. Zheng, X. Yang, Z.-Z. Shi, H. Ding, F. Pan and J.-F. Li, *J. Am. Chem. Soc.*, 2024, **146**, 26965–26974.
11 H. Li, Z. Huang, Y. Wang, G. Hai, W.-H. Huang, C.-C. Chang, M.-H. Yeh, F. Lai, N. Zhang and T. Liu, *Angew. Chem., Int. Ed.*, 2025, **64**, e202505156.
12 X. Liu, T. Xiang, J. Liu, B. Huang, Y. Yang, X. Qu, W. Xiong, M. Cheng, G. Jiang, Y. Liu and C. Zhou, *Adv. Funct. Mater.*, 2025, e21402.
13 G. Gan, G. Hong and W. Zhang, *Adv. Funct. Mater.*, 2025, **35**, 2401472.
14 Y. Li, L. Li, S. Xu, K. Cui, T. Wang, Z. Jiang and J. Li, *Angew. Chem., Int. Ed.*, 2024, **63**, e202407810.
15 K. Liu, H. Li, M. Xie, P. Wang, Z. Jin, Y. Liu, M. Zhou, P. Li and G. Yu, *J. Am. Chem. Soc.*, 2024, **146**, 7779–7790.
16 X. Zhu, Y.-C. Wang, K. Qu, L. Song, J. Wang, Y. Gong, X. Liu, C.-F. Li, S. Yuan, Q. Lu and A.-L. Wang, *Nat. Commun.*, 2025, **16**, 5742.
17 Y. Ma, S. Liu, J. Mao, M. Sun, K. Shi, W. Li, W. Zhao, J. Shan, Y. Zhao, Z. Jiang, R. Zhang, R. Gao, W. Liu, B. Huang, G. Q. M. Lu, J. Liu and L. Wu, *Nat. Mater.*, 2026, **25**, 80–90.
18 W. Chen, Z. Sun, S. Zhen, Y. Wang, J. Sun, M. Liu, W.-J. Han, L. Lai, W. Wei, L. Zhang and W. Chen, *Adv. Funct. Mater.*, 2025, e09200.
19 W. Mei, C.-W. Chang, Z. Li, X. Wang, Y. Qie, Q. Liu, R. C. Davis, Z. Wu, Y. Yue, C. Yang, S. Li, D. Han, Q.-H. Yang, Z. Feng and Z. Weng, *Adv. Mater.*, 2025, 2507363.
20 H. Zhao, P. Liu, X. Cheng, C. Fan, J. Liu, D. Kan and Y.-Q. Wang, *Adv. Funct. Mater.*, 2025, **35**, 2425459.
21 N. Li, C. Pan, G. Lu, H. Pan, Y. Han, K. Wang, P. Jin, Q. Liu and J. Jiang, *Adv. Mater.*, 2023, 2311023.
22 Z. Zhou, T. Ma, H. Zhang, S. Chheda, H. Li, K. Wang, S. Ehrling, R. Giovine, G. Li, A. H. Alawadhi and O. M. Yaghi, *Nature*, 2024, **635**, 96–101.
23 X. Li, S. Xia, S. Yang, X. Yang, S. Zheng, X. Xu, Y. Wang, Q. Xu and Z. Jiang, *Angew. Chem., Int. Ed.*, 2025, **64**, e202507479.
24 Y. Sun, W. Duan, J. Wang, P. Sun, Y. Zhang and Z. Li, *Chem. Sci.*, 2025, **16**, 9951–9965.
25 M. Chen, Z. Zhu, Y. Ji, X. Kong, D. Han and L. Zhai, *Chem. Sci.*, 2025, **16**, 11669–11677.
26 H. Li, M. Cao, Z. Fu, Q. Ma, L. Zhang, R. Wang, F. Liang, T. Zhou and C. Zhang, *Chem. Sci.*, 2024, **15**, 4341–4348.
27 J. Xiong, Q. An, H. Xiang, Y. Zhou, Y. Zhang, W. Chen, B. Ren, S. Wang, H. Bai, H. Guo and X. Yang, *Chem. Sci.*, 2026, **17**, 436–447.
28 Y. Song and S. Ma, *Chem. Sci.*, 2025, **16**, 11740.
29 Z. Liang, H.-Y. Wang, H. Zheng, W. Zhang and R. Cao, *Chem. Soc. Rev.*, 2021, **50**, 2540.
30 T. Sun, Z. Wang, Y. Wang, Q. Xu, K. Wang and J. Jiang, *Angew. Chem., Int. Ed.*, 2025, **64**, e202422814.
31 J. Dong, Y. Wang, Y.-L. Lu and L. Zhang, *Chin. Chem. Lett.*, 2023, **34**, 108052.
32 S. Li, W. Deng, Y. Wang, C. Zhao and Li. Zhang, *Appl. Mater. Today*, 2025, **47**, 102924.
33 H. Lin, Q. Mo, Y. Wang, C. Chen and L. Zhang, *Inorg. Chem.*, 2025, **64**, 2669–2680.
34 Q. Mo, C. Chen, S. Li, H. Song and L. Zhang, *Nano Res.*, 2025, **18**, 94907893.
35 Q. Mo, C. Chen, S. Li, H. Song and L. Zhang, *Small*, 2025, **21**, 2411926.
36 Z. Zhang, M. Wang, H.-R. Xing, X. Zhou, L. Gao, S. Chen, Y. Chen, H. Xu, W. Li, S. Yuan, C.-H. Li, Z. Jin and J.-L. Zuo, *Angew. Chem., Int. Ed.*, 2025, e202505580.
37 H. Hu, R. Miao, F. Yang, F. Duan, H. Zhu, Y. Hu, M. Du and S. Lu, *Adv. Energy Mater.*, 2024, **14**, 2302608.
38 B. Zhang, Y. Chen, Z. Dai, M. Cheng, P. Feng, B. Ke and G. Zhang, *Angew. Chem., Int. Ed.*, 2025, e21064.
39 J.-Y. Fang, Q.-Z. Zheng, Y. Y. Lou, K.-M. Zhao, S.-N. Hu, G. Li, O. Akdim, X.-Y. Huang and S.-G. Sun, *Nat. Commun.*, 2022, **13**, 7899.
40 S. Han, H. Li, T. Li, F. Chen, R. Yang, Y. Yu and B. Zhang, *Nat. Catal.*, 2023, **6**, 402–414.
41 Y. Xiao, X. Tan, B. Du, Y. Guo, W. He, H. Cui and C. Wang, *Angew. Chem., Int. Ed.*, 2024, **63**, e202408758.